Three-dimensional position and shape of the bow shock and their variation with upstream Mach numbers and interplanetary magnetic field orientation

J. Merka
L-3 Communications Government Services, Inc., Vienna, Virginia, USA

A. Szabo and J. A. Slavin
NASA Goddard Space Flight Center, Laboratory for Solar and Space Physics, Greenbelt, Maryland, USA

M. Peredo
Science Systems and Applications, Inc., Lanham, Maryland, USA

Received 1 December 2004; revised 10 January 2005; accepted 25 January 2005; published 7 April 2005.

[1] Peredo et al. (1995) derived a frequently used three-dimensional bow shock model parameterized by the upstream Alfvénic Mach number from the set of approximately 550 bow shock crossings provided by 17 distinct spacecraft over the period of 1963–1980. However, several studies reported some systematic biases in the bow shock model predictions. Therefore we have attempted to improve upon the bow shock model of Peredo et al. (1995) using their original data set and methodology in an effort to better understand these effects. We have performed three-dimensional best fits to the bow shock crossings binned by the upstream Mach numbers M_A, M_S, and M_{MS} and found that the best fitting surfaces were best ordered with the M_A. In agreement with predictions from the magnetohydrodynamic theory, the results show that the bow shock surface expands when the M_A decreases. The found dawn-dusk asymmetry in the bow wave is consistent with previous studies only in the Geocentric Plasma Ecliptic System (GPE) coordinates but not in the Geocentric Interplanetary Medium (GIPM) coordinates which suggests that the employed data set is not comprehensive enough for resolving this asymmetry. Nor is the Mach cone asymmetry resolved in our data set (not even in the GIPM frame). We have derived two models predicting the statistical position and shape of the bow shock in the GPE or GIPM coordinates. Error analysis shows that the GPE-based model is more accurate and applicable for $M_A = 3–20$ except the nose region where the model underestimates the bow shock position for $M_A < 5$. A direct comparison of the model predictions with 5870 IMP 8 bow shock crossings demonstrated high accuracy of predictions and, for the GPE-based model, an exceptional stability of predictions even under extreme upstream conditions. Indeed, the new GPE-based bow shock model is more accurate and equally or more stable than the Formisano (1979), Němeček and Šafránková (1991), Farris and Russell (1994), Cairns and Lyon (1995), Peredo et al. (1995), or Verigin et al. (2001) models.

Citation: Merka, J., A. Szabo, J. A. Slavin, and M. Peredo (2005), Three-dimensional position and shape of the bow shock and their variation with upstream Mach numbers and interplanetary magnetic field orientation, *J. Geophys. Res.*, *110*, A04202, doi:10.1029/2004JA010944.

1. Introduction

[2] Interaction of the supersonic solar wind with Earth's magnetosphere (magnetopause) creates fast mode magnetosonic waves that travel back upstream, combine and steepen to form the bow shock wave. The bow shock formation, position and variations have been extensively studied and modeled for more than four decades [e.g. *Walters*, 1964; *Spreiter et al.*, 1966; *Binsack and Vasyliunas*, 1968; *Fairfield*, 1971; *Spreiter and Rizzi*, 1974; *Formisano*, 1979; *Slavin and Holzer*, 1981; *Slavin et al.*, 1984, 1996; *Farris et al.*, 1991; *Němeček and Šafránková*, 1991; *Farris and Russell*, 1994; *Cairns and Grabbe*, 1994; *Cairns et al.*, 1995; *Cairns and Lyon*, 1995, 1996; *Peredo et al.*, 1995; *Bennett et al.*, 1997; *Petrinec and Russell*, 1997; *De Sterck et al.*, 1998;

Copyright 2005 by the American Geophysical Union.
0148-0227/05/2004JA010944

Fairfield et al., 2001; *Verigin et al.*, 2001, 2003; *Chao et al.*, 2002; *Chapman and Cairns*, 2003; *Dmitriev et al.*, 2003; *Chapman et al.*, 2004; *Merka and Szabo*, 2004]. Many of the previous investigations revealed that the bow shock shape and position are controlled primarily by solar wind ram pressure p_{sw} [*Binsack and Vasyliunas*, 1968; *Formisano*, 1979], by upstream Mach number(s) [e.g., *Spreiter et al.*, 1966; *Slavin and Holzer*, 1981; *Farris and Russell*, 1994; *Cairns and Grabbe*, 1994; *Fairfield et al.*, 2001; *Verigin et al.*, 2003; *Chapman and Cairns*, 2003; *Chapman et al.*, 2004], and by the orientation of the interplanetary magnetic field (IMF) [*Spreiter and Rizzi*, 1974; *Slavin et al.*, 1984, 1996; *De Sterck et al.*, 1998; *Kabin*, 2001; *Merka et al.*, 2003b; *Verigin et al.*, 2003; *Chapman et al.*, 2004].

[3] The bow shock model developed by *Fairfield* [1971], perhaps the first widely used empirical bow shock model, represents the average shape and position of the Earth's bow shock. The model is, however, based only on observations made near the ecliptic plane; thus the model is two-dimensional in that it assumes axial symmetry about the solar wind flow direction. Furthermore, *Fairfield* [1971] did not include any corrections to compensate for variations in solar wind dynamic pressure. *Formisano* [1979] derived a set of fully three-dimensional bow shock models. However, the data set was dominated by a very large number of often closely spaced HEOS 2 crossings (1980 crossings out of a total 2499), thus introducing a bias toward high-latitude observations and the HEOS 2 orbit. *Formisano* [1979] addressed the bias by introducing a weighting function but the technique remained controversial. However, recent comparative studies of bow shock models justified this technique and concluded that Formisano's model is quite accurate and often performs better than newer bow shock models [see *Šafránková et al.*, 1999; *Merka et al.*, 2003a, 2005].

[4] *Slavin and Holzer* [1981] and *Slavin et al.* [1983, 1984] added significantly to the bow shock crossing database of Fairfield and Formisano, but concentrated upon two-dimensional models for the purpose of examining Mach number effects on shock position and making comparisons with geodynamics theory. *Peredo et al.* [1995] employed this data set to produce three-dimensional models for bow shock shape and position that take into account variations in the solar wind dynamic pressure p_{sw}, in the upstream Mach numbers (sonic, Alfvénic, and magnetosonic Mach numbers, M_S, M_A, and M_{MS}, respectively), as well as the orientation of the IMF.

[5] The bow shock model by *Peredo et al.* [1995] has been frequently used even though its prediction is biased by at least 20% [*Šafránková et al.*, 1999; *Merka et al.*, 2003a, 2005]. Troubled by this deficiency, we have investigated original documents and found significant discrepancies in the satellite (bow shock) positions used for the preparation of the model. Thus, the purpose of this paper is to produce three-dimensional bow shock model(s) by employing the data set (with corrected positions) and methodology of *Peredo et al.* [1995].

[6] The approach of *Peredo et al.* [1995], i.e., fitting a second-order surface to the bow shock crossings binned by upstream conditions, is very straightforward and eliminates many assumptions and limitations inherent in other, even more recent, bow shock models. For example, models by *Farris and Russell* [1994] and *Cairns and Lyon* [1995] predict only the subsolar point magnetosheath thickness and the formulae provided by both of these models are empirical whether they are based on thoughtful theoretical arguments [*Farris and Russell*, 1994] or numerical modeling [*Cairns and Lyon*, 1995]. More recent bow shock models [e.g., *Verigin et al.*, 2001; *Chapman and Cairns*, 2003] base the bow shock shape on fits to results from supersonic gas flow experiments [*Verigin et al.*, 2001] and/or numerical magnetohydrodynamic (MHD) simulations [*Chapman and Cairns*, 2003]. Each approach contains severe limitations: The gas flow often differs from the magnetized plasma flow; the MHD simulations assume an impermeable infinitely conducting magnetopause obstacle which is far from reality. On the other hand, the most severe limitation, when fitting a surface to an existing database of bow shock crossings, is the number and distribution of data points available as will be discussed in the paper. Indeed, the more data points available, the less restrictions have to be placed on the parameterization of the fitted surface(s).

[7] The present paper reprocesses the bow shock crossing database employed by *Peredo et al.* [1995] using their methodology. In addition to that, an error analysis is performed in order to allow a discussion of confidence limits of the resulting models. The error analysis provides evidence that, for example, the three-dimensional fits for Alfvénic Mach numbers $M_A < 5$ are significantly less reliable due to the sparse data set. The derived models are compared with IMP 8 bow shock observations to facilitate a direct comparison with other bow shock models tested by *Merka et al.* [2005]. The results show that the newly derived bow shock models are of similar accuracy as other current models. Furthermore, the new models perform better for unusual upstream conditions.

[8] The remainder of this paper is organized as follows: Key characteristics of the data set are described in section 2. The data analysis techniques, fitting procedures, and results are presented in section 3. Results from the analysis and comparison with results from *Peredo et al.* [1995] appear in sections 4.1 and 4.2, while the performance of the new models and comparison with results of *Merka et al.* [2005] are presented in section 4.3. The summary and conclusions appear in section 5.

2. Data Set

[9] The genesis and evolution of the bow shock list employed in this study is quite complicated because several researchers extended and processed the data set during more than two decades [e.g., *Fairfield*, 1971; *Formisano*, 1979; *Slavin and Holzer*, 1981; *Slavin et al.*, 1983, 1984; *Peredo et al.*, 1995]. Our data set, which is practically identical to the set used by *Peredo et al.* [1995], includes a collection of 1492 bow shock crossings observed by 17 different spacecraft between November 1963 and November 1980 (see Table 1). However, only 570 crossings were used due to the limited availability of upstream parameters. The upstream parameters were obtained from the OMNI2 database of hourly averaged solar wind and interplanetary magnetic field (IMF) data produced by the National Space Science Data Center (NSSDC). Sonic, Alfvénic, and magnetosonic

Table 1. Numbers of Available and Used Bow Shock Crossings[a]

Spacecraft	Dates	Data	Used
IMP 1	Nov. 63–Feb. 64	30	-
OGO 1	Nov. 64–Dec. 64	9	-
IMP 3	June 65–Jan. 67	124	17
EXP 33	Nov. 66–May 68	48	18
IMP 4	June 67–Dec. 68	160	48
EXP 35	July 67–Sept. 68	21	15
OGO 5	March 68–March 69	83	37
HEOS 1	Dec. 68–Jan. 70	144	22
HEOS 2	Feb. 72–Dec. 73	262	119
Prognoz 1	April 72–Aug. 72	64	27
Prognoz 2	June 72–Nov. 72	59	8
IMP 8	Nov. 73–Nov. 80	224	72
IMP 6	Jan. 74–July 74	108	82
Prognoz 4	Jan. 76–March 76	29	17
Prognoz 5	Nov. 76–April 77	59	30
ISEE 1	Oct. 77–Sept. 79	42	33
Prognoz 7	Nov. 78–Jan. 79	26	25
Total		1492	570

[a]The number of bow shock crossings used in the present study is limited by the availability of the upstream parameters.

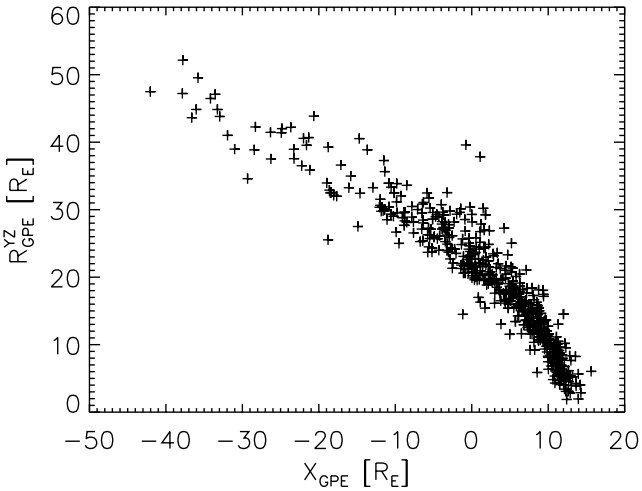

Figure 2. Distribution of bow shock crossings in a cylindrical projection of the GPE coordinates. The positions are scaled to the average ram pressure.

Mach numbers (M_S, M_A, and M_{MS}) were computed from the solar wind and IMF data and merged with the bow shock crossings to produce a data set containing the location and time of the crossings, solar wind and IMF parameters, and Mach numbers.

[10] The aberration due to the Earth's orbital motion has been removed from the bow shock positions. The nonradial component of the solar wind velocity is unknown so we assume purely radial solar wind flow. Therefore, the used frame of reference can be called the Geocentric Plasma Ecliptic System (GPE) as defined by *Merka and Szabo* [2004]. Figure 1 illustrates the distribution of the 570 crossings in GPE longitude and latitude, while Figure 2 shows a cylindrical projection of the entire data set. Figure 1 clearly demonstrates that the data set consists predominantly of northern hemisphere crossings and that the number of crossings for latitudes below −50° is close to zero. Note that many data points, namely the HEOS 2 and IMP 8 subsets, have been obtained by averaging positions of several bow shock crossings observed within dozens of minutes or even several hours. Although this approach is quite subjective, it was deemed to be necessary in order to eliminate, or at least to decrease, biases due to shock-skimming spacecraft orbits which provide significantly larger number of crossings than other orbits. In Figure 1, the void around longitudes ±180° corresponds to the magnetosphere, so no crossings are present in that region.

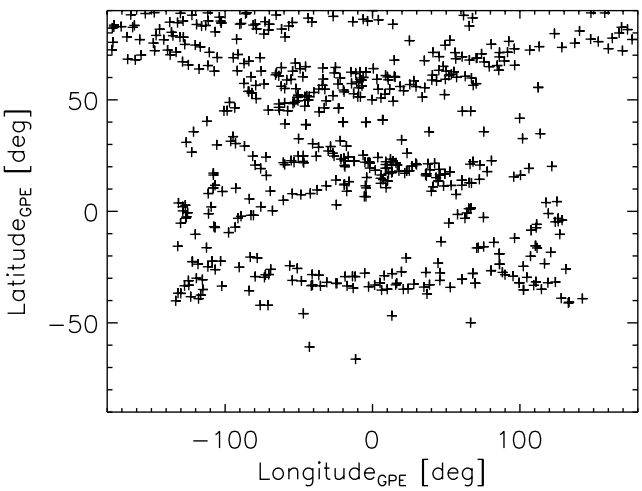

Figure 1. Distribution of bow shock crossings in GPE longitude and latitude.

[11] In order to test the newly designed bow shock models, we also employed the extensive IMP 8 bow shock list which contains 5870 unambiguous bow shock crossings with upstream magnetic field and plasma parameters [*Merka et al.*, 2005].

3. Method of Analysis

[12] The present study employs substantially the same technique as described by *Peredo et al.* [1995] and adds to it an error analysis of the bow shock fits. For the reader's convenience, we describe the entire method here again and highlight new extensions and modifications.

[13] In order to establish the average position and shape of the bow shock for different solar wind and IMF conditions, we attempt to remove effects due to upstream conditions one at a time. First, effects associated with the Earth's orbital motion are removed by rotating into the GPE coordinates as noted in the previous section. The solar wind dynamic pressure scales the entire bow shock [e.g., *Binsack and Vasyliunas*, 1968; *Formisano*, 1979]. We account for the solar wind variations by performing a normalization of all crossings to the average ram pressure for our data set according to the relation [e.g., *Spreiter et al.*, 1966; *Fairfield*, 1971; *Holzer and Slavin*, 1978]:

$$r_n = r_o \left(\frac{n_o v_o^2}{n_a v_a^2} \right)^{\frac{1}{6}} \tag{1}$$

where r_n and r_o are the normalized and observed distances to a bow shock crossing, respectively; n_o, n_a, v_o and v_a are, respectively, the observed and average solar wind number

densities and bulk speeds. The average quantities for our data set are n_a = 7.0 cm^{-3}, and v_a = 457.5 km/s.

[14] Upon removal of the solar wind dynamic pressure effects, we binned the data independently into four ranges of M_A (2–5, 5–8, 8–13, and 13–20), three ranges of M_S (5–7, 7–8, and 8–10), and three ranges of M_{MS} (2–5, 5–6, 6–9). Best fitting three-dimensional second-order bow shock curves were then derived for each subset according to the following procedure. A general second-order surface may be described by the expression

$$\begin{aligned} F(x,y,z) &= a_1x^2 + a_2y^2 + a_3z^2 \\ &\quad + 2a_4xy + 2a_5yz + 2a_6xz \\ &\quad + 2a_7x + 2a_8y + 2a_9z + a_{10} \\ &= 0 \end{aligned} \tag{2}$$

where $\vec{r}$ = (x, y, z) is the position, in GPE coordinates, of a point on the bow shock surface; the free parameters ($a_1 \ldots a_{10}$) are determined by minimizing the root squared distance between the observed crossings and the surface. Thus, the task is to minimize the merit function χ^2 defined by the relation

$$\chi^2 = \sum_{i=1}^{N} \left[\frac{F_i}{\nabla F_i} \right]^2 \tag{3}$$

where N is the number of crossings at positions $\vec{r}_i$ = (x_i, y_i, z_i). It must be noted that the approach of *Peredo et al.* [1995] to minimize the distance normal to the boundary is rather novel and rare in bow shock studies. Other studies usually minimize the distance to the boundary along one direction (e.g., in the direction of increasing z, or of increasing $(y^2 + z^2)^{1/2}$ for axially symmetric models).

[15] The minimization of the merit function χ^2 is accomplished by the Levenberg-Marquardt method [*Marquardt*, 1963] for nonlinear least squares fitting. For more details about the implementation of the fitting method, the reader is referred to Appendix B of *Peredo et al.* [1993] and section 2 of *Peredo et al.* [1995].

[16] *Peredo et al.* [1995] assumed north-south symmetry of the fitted bow shock surface, and set the coefficients a_5, a_6, and a_9 identically equal to zero because of a lack of crossings with latitude below −50°. Furthermore, they set a_2 = 1. In order to closely follow the method of *Peredo et al.* [1995], the results presented below are also limited to bow shock shapes which assume north-south symmetry.

[17] To separate variability due to IMF and Mach number effects, both *Peredo et al.* [1995] and the present study rotate all bow shock crossings into Geocentric Interplanetary Medium (GIPM) coordinates [*Bieber and Stone*, 1979] where the B_z component of the IMF vanishes. The resulting data set was again binned according to M_A, M_S, and M_{MS} values and new best fitting surfaces were derived.

[18] Every fitting procedure should be accompanied by an error analysis which establishes confidence limits of the results. The original work of *Peredo et al.* [1995] lacked a thorough error analysis. Thus, the present study estimates the standard errors of the fitted parameters a_1, a_3, a_4, a_7, a_8, and a_{10} by the bootstrap method proposed by *Efron* [1979]. The bootstrap method is a general methodology for nonparametrically estimating the statistical errors and the implementation is quite straightforward [see *Kawano and Higuchi*, 1995]. There remains one ad hoc parameter for an actual application of the bootstrap method, namely the number of bootstrap trials M. The number of bootstrap trials usually does not exceed 2000 [*Kawano and Higuchi*, 1995, and references therein] and this number is used in the present study.

4. Results

4.1. Fitted Bow Shock Surfaces

[19] The parameters a_i characterizing the best fitting bow shock curves are listed in Table 2 including their standard errors estimated by the bootstrap method. Based on the a_i parameters, we provide the key dimensions of the fitted bow shock surfaces in a more intuitive form in Table 3. For each of the data subsets, Table 3 lists the number of bow shock crossings in the subset, N; the intersection with the axis, x_{nose}, y_{dusk}, y_{dawn}, and z_{north}; and three asymmetry ratios, $y_{\mathrm{dusk}}/|y_{\mathrm{dawn}}|$, $y_{\mathrm{dusk}}/z_{\mathrm{north}}$, and $|y_{\mathrm{dawn}}|/z_{\mathrm{north}}$, describing the axial asymmetry of the resulting bow shock surfaces. Individual fits were generated for each bin in M_A, M_S, or M_{MS} and for the combined sets for each of these Mach numbers. The top portions of Tables 2 and 3 correspond to the sets that were normalized to the average pressure according to equation 1 and rotated into GPE coordinates to remove solar wind flow aberration effects, while the bottom halves of the tables correspond to sets that were pressure normalized and rotated into GIPM coordinates to remove effects due to orientation of the IMF.

[20] The uncertainties in all parameters, calculated from the fitted parameters a_i, are estimated via propagation of error formulas [e.g., *Ku* 1966]. The propagation of the error formula for a function $g = f(x, y, \ldots)$ of one or more variables x, y,... gives the following estimate for the standard deviation of g:

$$\sigma_g^2 = \left(\frac{\partial f}{\partial x}\right)^2 \sigma_x^2 + \left(\frac{\partial f}{\partial y}\right)^2 \sigma_y^2 + \ldots + \frac{\partial f}{\partial x}\frac{\partial f}{\partial y}\sigma_{xy}^2 + \ldots \tag{4}$$

where σ_x and σ_y are the standard deviations of x and y, respectively, and σ_{xy} is the estimated covariance between x and y variables. We did not include the covariance terms because of a lack of sufficient data to estimate them (see *Ku* [1966] for guidance on what constitutes sufficient data).

[21] The effect of varying M_A on the bow shock shape and position in GPE coordinates is shown in Figures 3, 4, and 5, where projections of the best fitting bow shock surfaces are shown for the equatorial, noon-midnight, and terminator planes, respectively, for several ranges of M_A. The projections of the shock surfaces in the terminator plane are also presented in the GIPM coordinates in Figure 6. In these figures, we also present projections of bow shock crossings from the M_A = 2–5 set within 5 R_E of the respective plane, and show a 1 standard deviation uncertainty region from the bow shock surface. We chose the M_A = 2–5 data set in order to illustrate that, for this subset, the irregular spatial distribution of the data points results in a rather ambiguous bow shock surface fit. Notice, for example, the peculiar flaring at the dawn side in Figure 3 or the rapid increase of the standard error tailward. We attribute both effects to the use of a rather sparse and irregular data set. It is

Table 2. Parameters for Best Fitting Bow Shock Surfaces for Various M_A, M_S, and M_{MS} Conditions

Subset		a_1	a_3	a_4	a_7	a_8	a_{10}
				GPE Coordinates			
M_A	2–5	−0.12292 ± 0.57716	0.81092 ± 0.11429	−0.20902 ± 0.14660	28.270 ± 2.966	−0.75985 ± 0.96604	−649.29 ± 36.19
	5–8	−0.02996 ± 0.05664	0.93743 ± 0.05399	0.00227 ± 0.02399	21.196 ± 0.697	−0.57751 ± 0.30654	−536.81 ± 18.35
	8–13	−0.21644 ± 0.09335	0.91729 ± 0.05016	0.01680 ± 0.03805	19.570 ± 0.914	0.02222 ± 0.28772	−471.21 ± 21.97
	13–20	0.04615 ± 0.19012	1.00468 ± 0.08448	0.01286 ± 0.06630	20.280 ± 1.200	−0.03024 ± 0.46548	−512.18 ± 27.12
	2–20	−0.04766 ± 0.04981	0.94784 ± 0.03655	0.00761 ± 0.01723	21.034 ± 0.553	−0.31152 ± 0.20116	−524.03 ± 14.65
M_S	5–7	−0.27495 ± 0.11823	0.83983 ± 0.06709	0.03671 ± 0.04994	20.676 ± 1.168	−0.59740 ± 0.45694	−485.57 ± 28.02
	7–8	−0.13808 ± 0.10356	0.93524 ± 0.06264	0.00711 ± 0.03584	19.949 ± 0.966	−0.05226 ± 0.33378	−496.94 ± 26.24
	8–10	0.02125 ± 0.08849	0.99005 ± 0.05001	0.02538 ± 0.02678	20.943 ± 0.632	−0.33222 ± 0.27580	−525.14 ± 16.65
	5–10	−0.12758 ± 0.05421	0.90944 ± 0.03617	0.01760 ± 0.01734	20.351 ± 0.527	−0.29289 ± 0.19904	−499.62 ± 14.52
M_{MS}	2–5	0.02089 ± 0.09657	0.86985 ± 0.06654	−0.02636 ± 0.03904	21.566 ± 0.932	−0.71127 ± 0.42788	−546.94 ± 24.71
	5–6	−0.22326 ± 0.05686	0.93978 ± 0.04479	0.04812 ± 0.01906	20.536 ± 0.587	−0.32243 ± 0.27833	−499.42 ± 16.28
	6–9	−0.01455 ± 0.10758	0.91866 ± 0.05108	−0.02715 ± 0.03980	19.053 ± 0.869	−0.16600 ± 0.29321	−476.28 ± 21.67
	2–9	−0.04747 ± 0.05153	0.95009 ± 0.03592	0.01018 ± 0.01737	20.959 ± 0.551	−0.37395 ± 0.20206	−521.72 ± 14.85
				GIPM Coordinates			
M_A	2–5	0.11016 ± 0.66823	1.12084 ± 0.13788	0.15574 ± 0.22337	30.124 ± 5.189	0.57159 ± 1.25443	−744.04 ± 63.95
	5–8	0.03033 ± 0.06327	0.89212 ± 0.05361	−0.00075 ± 0.03166	20.413 ± 0.872	0.01593 ± 0.31484	−522.94 ± 21.54
	8–13	−0.10281 ± 0.08835	1.02440 ± 0.06643	−0.02318 ± 0.03601	20.839 ± 0.916	0.54211 ± 0.25349	−512.86 ± 22.80
	13–20	−0.00835 ± 0.18655	1.14550 ± 0.09652	0.05188 ± 0.06135	21.537 ± 1.385	−0.60097 ± 0.55547	−546.88 ± 32.75
	2–20	−0.01663 ± 0.04247	0.98133 ± 0.03981	−0.00800 ± 0.01931	21.147 ± 0.586	0.20428 ± 0.20098	−532.21 ± 14.66
M_S	5–7	−0.04622 ± 0.08829	0.87544 ± 0.06247	−0.03965 ± 0.04587	20.645 ± 1.251	−0.06869 ± 0.46986	−511.36 ± 28.99
	7–8	−0.06953 ± 0.08001	1.00212 ± 0.06691	−0.03674 ± 0.03516	20.664 ± 1.021	−0.06742 ± 0.27145	−523.12 ± 23.96
	8–10	0.01846 ± 0.07330	1.04977 ± 0.07122	0.03328 ± 0.03053	21.479 ± 0.784	0.77266 ± 0.29949	−537.66 ± 21.48
	5–10	−0.02547 ± 0.04634	0.97659 ± 0.03809	−0.00660 ± 0.01850	20.950 ± 0.562	0.17438 ± 0.19552	−526.03 ± 13.97
M_{MS}	2–5	0.22505 ± 0.10446	0.94307 ± 0.07333	0.01017 ± 0.05517	22.593 ± 1.452	0.21240 ± 0.50298	−585.90 ± 33.18
	5–6	−0.15450 ± 0.05208	0.95938 ± 0.04679	0.00500 ± 0.02482	20.556 ± 0.689	0.01043 ± 0.24338	−509.26 ± 15.72
	6–9	0.00192 ± 0.11535	1.04887 ± 0.06302	0.00345 ± 0.03946	20.278 ± 0.834	0.44115 ± 0.28023	−510.95 ± 22.61
	2–9	−0.01458 ± 0.04249	0.99424 ± 0.03767	−0.00859 ± 0.01902	21.176 ± 0.565	0.21311 ± 0.19729	−532.81 ± 13.85

essential to understand that the fitting procedure will (practically) always find a best fitting surface for a given data set and it is our responsibility to supply a data set well representing the sought surface or the resulting fit may be unrealistic, yet still an accurate fit. Thus for the larger data sets (the higher Mach number subsets), the fitting procedure provides much more reliable fits with significantly smaller uncertainties (see Table 3).

[22] From Figures 3 and 4 (and values in Table 3), we find that the bow shock stand-off distance (the nose) moves slightly earthward with decreasing M_A, while the flaring of the bow wave increases. This result qualitatively agrees

Table 3. Characteristic Dimensions of Bow Shock Fits for Various M_A, M_S, and M_{MS} Conditions

Subset		N	x_{nose} [R_E]	y_{dusk} [R_E]	y_{dawn} [R_E]	z_{north} [R_E]	$y_{dusk}/\lvert y_{dawn}\rvert$	y_{dusk}/z_{north}	$\lvert y_{dawn}\rvert/z_{north}$
					GPE Coordinates				
M_A	2–5	57	11.8 ± 2.1	26.3 ± 1.2	−24.7 ± 1.2	28.3 ± 2.1	1.061 ± 0.005	0.928 ± 0.007	0.874 ± 0.006
	5–8	198	12.8 ± 0.7	23.8 ± 0.5	−22.6 ± 0.5	23.9 ± 0.8	1.051 ± 0.001	0.993 ± 0.002	0.944 ± 0.001
	8–13	235	13.0 ± 1.1	21.7 ± 0.6	−21.7 ± 0.6	22.7 ± 0.8	0.998 ± 0.001	0.957 ± 0.002	0.959 ± 0.002
	13–20	60	12.5 ± 1.2	22.7 ± 0.8	−22.6 ± 0.8	22.6 ± 1.1	1.003 ± 0.002	1.004 ± 0.004	1.001 ± 0.004
	2–20	550	12.6 ± 0.5	23.2 ± 0.4	−22.6 ± 0.4	23.5 ± 0.6	1.028 ± 0.001	0.987 ± 0.001	0.960 ± 0.001
M_S	5–7	157	12.8 ± 1.3	22.6 ± 0.8	−21.4 ± 0.8	24.0 ± 1.2	1.056 ± 0.003	0.942 ± 0.003	0.892 ± 0.003
	7–8	209	13.0 ± 1.1	22.3 ± 0.7	−22.2 ± 0.7	23.1 ± 1.0	1.005 ± 0.002	0.969 ± 0.003	0.965 ± 0.003
	8–10	179	12.5 ± 0.6	23.3 ± 0.5	−22.6 ± 0.5	23.0 ± 0.7	1.029 ± 0.001	1.010 ± 0.001	0.981 ± 0.001
	5–10	545	12.8 ± 0.6	22.6 ± 0.4	−22.1 ± 0.4	23.4 ± 0.6	1.027 ± 0.001	0.966 ± 0.001	0.941 ± 0.001
M_{MS}	2–5	177	12.6 ± 0.9	24.1 ± 0.7	−22.7 ± 0.7	25.1 ± 1.1	1.063 ± 0.002	0.961 ± 0.003	0.905 ± 0.002
	5–6	184	13.1 ± 0.7	22.7 ± 0.5	−22.0 ± 0.5	23.1 ± 0.7	1.029 ± 0.001	0.984 ± 0.001	0.956 ± 0.001
	6–9	209	12.6 ± 0.9	22.0 ± 0.6	−21.7 ± 0.6	22.8 ± 0.8	1.015 ± 0.001	0.966 ± 0.002	0.951 ± 0.002
	2–9	570	12.6 ± 0.5	23.2 ± 0.4	−22.5 ± 0.4	23.4 ± 0.6	1.033 ± 0.001	0.991 ± 0.001	0.959 ± 0.001
					GIPM Coordinates				
M_A	2–5	57	12.1 ± 2.7	26.7 ± 1.7	−27.9 ± 1.7	25.8 ± 1.9	0.959 ± 0.007	1.037 ± 0.010	1.081 ± 0.011
	5–8	198	12.7 ± 0.8	22.9 ± 0.6	−22.9 ± 0.6	24.2 ± 0.9	0.999 ± 0.001	0.944 ± 0.002	0.945 ± 0.002
	8–13	235	12.7 ± 0.9	22.1 ± 0.6	−23.2 ± 0.6	22.4 ± 0.9	0.953 ± 0.001	0.988 ± 0.002	1.037 ± 0.002
	13–20	60	12.7 ± 1.3	24.0 ± 0.9	−22.8 ± 0.9	21.8 ± 1.1	1.053 ± 0.003	1.098 ± 0.005	1.043 ± 0.005
	2–20	550	12.6 ± 0.5	22.9 ± 0.4	−23.3 ± 0.4	23.3 ± 0.6	0.982 ± 0.001	0.982 ± 0.001	0.999 ± 0.001
M_S	5–7	157	12.6 ± 1.1	22.7 ± 0.8	−22.5 ± 0.8	24.2 ± 1.1	1.006 ± 0.003	0.938 ± 0.003	0.933 ± 0.003
	7–8	209	12.9 ± 1.0	22.9 ± 0.6	−22.8 ± 0.6	22.8 ± 0.9	1.006 ± 0.001	1.004 ± 0.002	0.998 ± 0.002
	8–10	179	12.4 ± 0.7	22.4 ± 0.5	−24.0 ± 0.6	22.6 ± 0.9	0.936 ± 0.001	0.991 ± 0.002	1.059 ± 0.002
	5–10	545	12.7 ± 0.5	22.8 ± 0.4	−23.1 ± 0.4	23.2 ± 0.5	0.985 ± 0.000	0.981 ± 0.001	0.996 ± 0.001
M_{MS}	2–5	177	12.2 ± 1.0	24.0 ± 0.8	−24.4 ± 0.9	24.9 ± 1.2	0.983 ± 0.002	0.963 ± 0.003	0.980 ± 0.003
	5–6	184	13.0 ± 0.7	22.6 ± 0.4	−22.6 ± 0.4	23.0 ± 0.7	0.999 ± 0.001	0.979 ± 0.001	0.980 ± 0.001
	6–9	209	12.6 ± 0.9	22.2 ± 0.6	−23.0 ± 0.6	22.1 ± 0.8	0.962 ± 0.001	1.004 ± 0.002	1.044 ± 0.002
	2–9	570	12.6 ± 0.5	22.9 ± 0.4	−23.3 ± 0.4	23.1 ± 0.5	0.982 ± 0.000	0.988 ± 0.001	1.006 ± 0.001

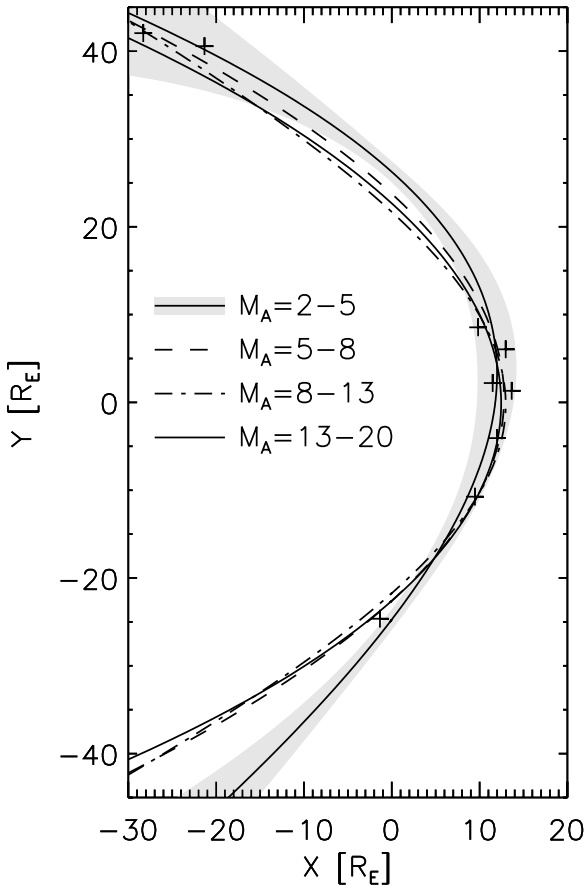

Figure 3. Comparison of the equatorial projection ($Z = 0$) of the best fitting bow shock curves for different ranges of M_A. These curves correspond to crossings that were pressure normalized and rotated into GPE coordinates. For the $M_A = 2-5$ bin, the corresponding data points within 5 R_E of the plane are displayed and the shaded band depicts one standard deviation uncertainty for the bow shock curve.

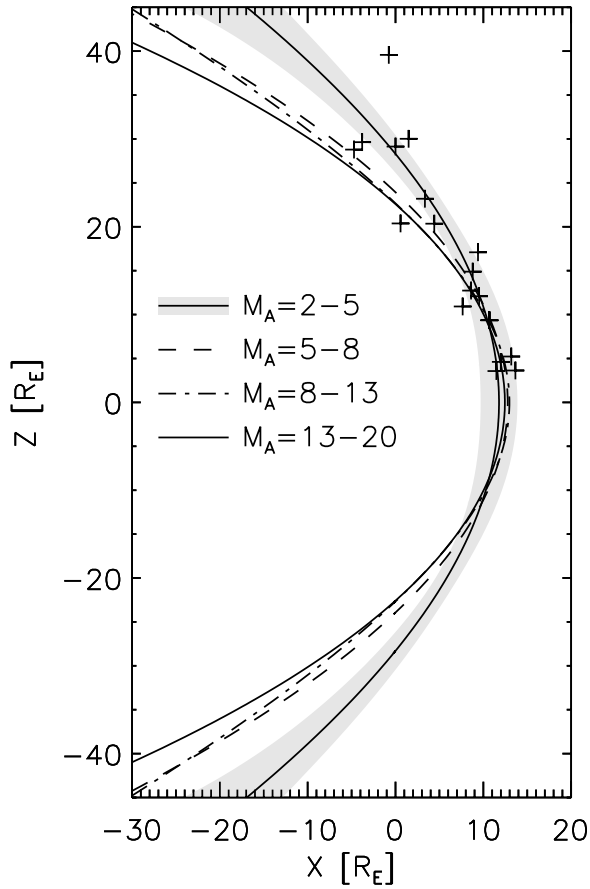

Figure 4. Same as Figure 3, but for the noon-midnight plane.

with *Peredo et al.* [1995]. However, upon closer scrutiny we find that the changes of the bow shock stand-off distance are well within one standard deviation error bar which means that the changes of x_{nose} for varying Mach numbers M_A, M_S, or M_{MS} are statistically unresolved (Table 3).

[23] At low Mach numbers, the shock wave becomes weaker and the entire shock is found farther from Earth so that the deflection of the solar wind flow around the obstacle can still occur [e.g., *Spreiter et al.*, 1966; *Farris and Russell*, 1994; *Cairns and Grabbe*, 1994; *Fairfield et al.*, 2001] but the results presented in Table 3 suggest approximately constant or slightly decreasing x_{nose}. It has been shown in MHD simulations [*Spreiter and Rizzi*, 1974; *Cairns and Lyon*, 1995; *De Sterck et al.*, 1998; *Kabin*, 2001; *Chapman et al.*, 2004] and observations [*Merka et al.*, 2003b] that the bow shock standoff distance can actually decrease with decreasing M_A when $\theta_{\mathrm{Bv}} \rightarrow 0°$ where θ_{Bv} is the angle between the IMF and solar wind velocity vectors. The IMF orientation of $\theta_{\mathrm{Bv}} < 20°$ is rather unusual and does not dominate our data set so we can exclude this effect. We propose to explain the found behavior of x_{nose} by the orbital bias skewing the resulting x_{nose} dependence on Mach numbers. There is a lack of spacecraft with orbits systematically covering the region at the bow shock nose at radial distances between approximately 15 and 30 R_E which is where we would expect the bow shock position for $M_A < 5$.

[24] *Peredo et al.* [1995] reported dawn-dusk bow shock asymmetries consistent with the asymmetry predicted by

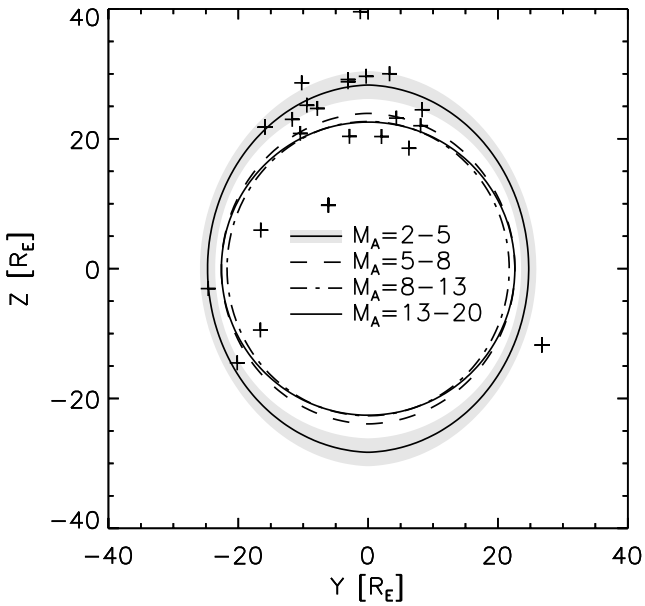

Figure 5. Same as Figure 3, but for the terminator plane.

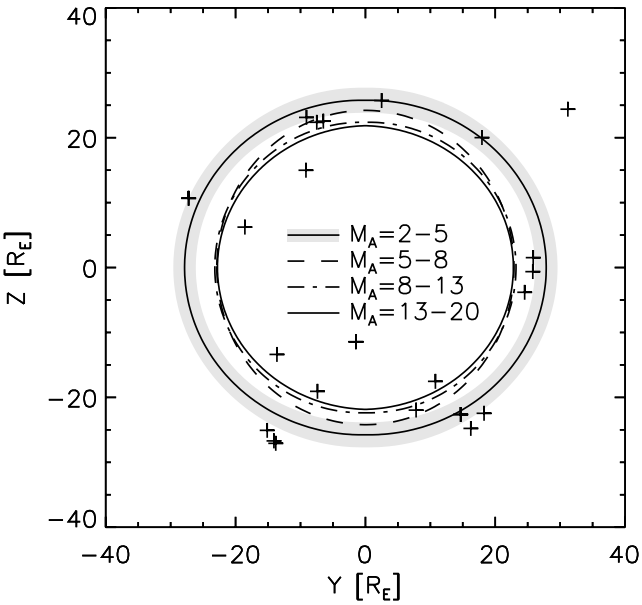

Figure 6. Same as Figure 5, but for the data rotated in the GIPM coordinates.

Walters [1964] as a consequence of the orientation of the IMF and asymmetries in the magnetic field line draping pattern. *Walters* [1964] predicted that for the IMF oriented along the Parker's spiral, the bow shock flares out more at the dusk flank than at the dawn flank. However, the dawn-dusk asymmetry displayed in Figures 5 and 6 and quantified in Table 3 qualitatively agree with the predicted effect only for the GPE data set. For the GIPM data set we indeed find an opposite dawn-dusk asymmetry. Note that the dawn-dusk asymmetry should be more apparent for the GIPM data set because in this coordinate system the IMF points exactly duskward in the *Y-Z* plane at all times.

[25] Theory and observations indicate that the bow shock asymptotically approaches the magnetosonic Mach cone [e.g., *Landau and Lifshitz*, 1959; *Romanov et al.*, 1978; *Slavin et al.*, 1984; *Spreiter and Stahara*, 1985; *Verigin et al.*, 2003]. Thus the bow shock cross section at large distances downstream from Earth resembles the outermost curve in the phase velocity diagram for the hydromagnetic waves, commonly known as a Friedrichs diagram [see *Peredo et al.*, 1995; *Verigin et al.*, 2003]. The most convenient coordinate system allowing to resolve the Mach cone asymmetries is the GIPM reference frame because the IMF points duskward in the *Y-Z* at all times. In contrast to the work of *Peredo et al.* [1995], we find that the north-south shock dimension is smaller than the dawn-dusk dimension in the terminator plane (Figure 6) which is indeed an opposite effect to a bow shock shape approaching the Mach cone (in GIPM coordinates the north-south dimension should be larger). *Slavin and Holzer* [1981] looked for this asymmetry in the Earth bow shock using IMP 4 crossings, but failed to find a significant effect. *Merka and Szabo* [2004] also failed to find a significant effect even though they scrutinized more than 2000 IMP 8 bow shock crossings. Interestingly, the ion flux in the magnetosheath also exhibits dawn-dusk asymmetry that does not appear to be controlled by the IMF [*Paularena et al.*, 2001; *Němeček et al.*, 2003], however we could not establish a direct connection of the magnetosheath asymmetry with the bow shock shape asymmetry found here. In agreement with *Slavin and Holzer* [1981] and *Merka and Szabo* [2004], we conclude that the bow shock's shape at the terminator is determined primarily by the obstacle's shape, and thus the Mach cone asymmetries are easily masked by uncertainties arising from irregular bow shock sampling and subset selection.

[26] The north-south dimension of the best fitting bow shock surfaces in GPE coordinates is up to 10% larger than the dawn-dusk dimension, while rotation into GIPM coordinates reduces this asymmetry by a few percent. The north-south intersection with the *Z* axis is well ordered with Mach numbers and decreases with increasing Mach numbers. On the other hand, the dawn-dusk dimension is less ordered with Mach numbers but still generally decreases with increasing Mach numbers.

[27] We conclude that of the three Mach numbers considered, the Alfvénic Mach number yields the better ordering of bow shock characteristics because it covers a wider range of values than the sonic and magnetosonic Mach numbers even though the ordering is comparable within the same value ranges of M_A, M_S, and M_{MS}. Contrary to the *Peredo et al.* [1995] study, we do not find that rotating into GIPM coordinates provides significant benefits: (1) the ordering is slightly worse than for GPE coordinates; and (2) the fits fail to resolve expected IMF effects.

4.2. New Bow Shock Models

[28] *Peredo et al.* [1995] derived a bow shock model explicitly parameterized by M_A for their set of bow shock crossings that was pressure-normalized and rotated into GIPM coordinates. They fitted a second-order polynomial through the bow shock surface parameters a_i (i = 1, 3, 4, 7, 8, 10) to describe the variations in a_i with M_A. However, the present study has not found sufficient justification for the use of the GIPM coordinates. Thus, we will derive new models for the sets of pressure normalized bow shock crossings in both GPE and GIPM coordinates.

[29] Figures 7 and 8 show the variations of a_i with M_A for the sets in GPE and GIPM coordinates. Note that for each M_A subset, the mean Alfvénic Mach number $\overline{M_A}$ and the standard deviation σ_{M_A} have been calculated. For the four M_A subsets in both the GPE and GIPM coordinates, the mean Alfvénic Mach numbers $\overline{M_A}$ are: 4.1 ± 0.8, 6.7 ± 0.8, 10.1 ± 1.4, and 15.6 ± 1.9. Thus, the diamonds representing values of the a_i parameters are located at $\overline{M_{Ai}}$ and the horizontal error bars represent one standard deviation interval around each $\overline{M_{Ai}}$. The vertical error bars show one standard deviation interval around each a_i.

[30] It is important to recognize that in spite of binning the data for quite wide intervals of M_A, the majority of data points falls within much narrower intervals. This is especially critical in the low M_A bin (2−5) where the bow shock response to the M_A changes is more pronounced than for higher Alfvénic Mach numbers. It would be a mistake to calculate the mean $\overline{M_A}$ based on the interval boundaries and not from the actual distribution of M_A within the particular subset.

[31] We have investigated several functional forms describing the variations in each a_i with M_A. Our goal was to

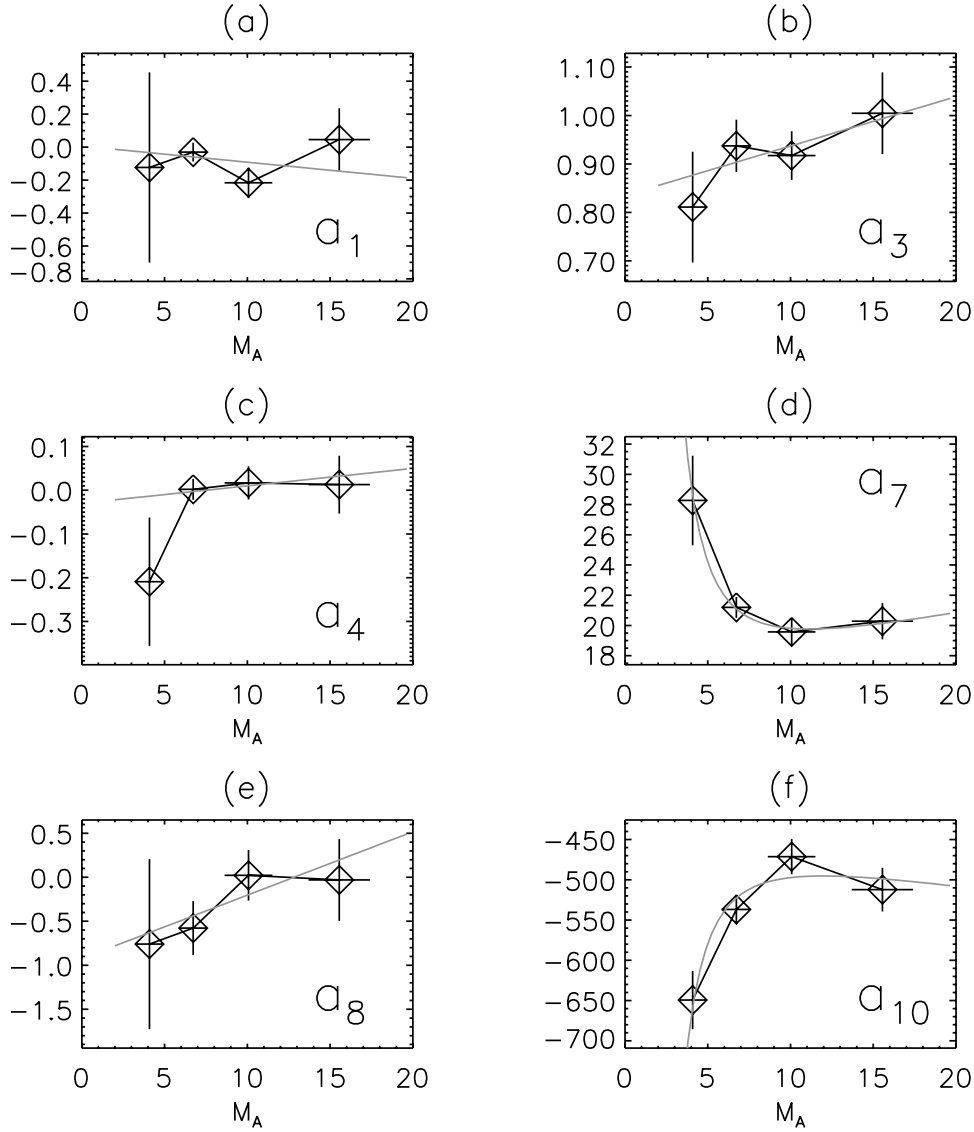

Figure 7. Dependence on Alfvénic Mach number M_A of the parameters a_1, a_3, a_4, a_7, a_8, and a_{10} for best fitting bow shock surfaces in GPE coordinates. The gray curves present best fits using functional forms defined by equation (5).

obtain simple functional forms while keeping the errors as little as possible. Finally, we chose to express the M_A control of the bow shock position and shape in the a_i parameters as

$$\begin{aligned} a_1 &= b_{1,1} + b_{1,2}M_A \\ a_3 &= b_{3,1} + b_{3,2}M_A \\ a_4 &= b_{4,1} + b_{4,2}M_A \\ a_7 &= b_{7,1} + b_{7,2}M_A + \frac{b_{7,3}}{(M_A - 1)^2} \\ a_8 &= b_{8,1} + b_{8,2}M_A \\ a_{10} &= b_{10,1} + b_{10,2}M_A + \frac{b_{10,3}}{(M_A - 1)^2} \end{aligned} \tag{5}$$

where the b_{ij} coefficients together with their uncertainties are summarized in Table 4. These functional forms are depicted as gray curves in Figures 7 and 8. Note that the chosen functional forms (5) are not physics-based except the functions for the a_7 and a_{10} parameters which were motivated by the fact that the shock should move to infinity when $M_A \rightarrow 1$ [*Landau and Lifshitz*, 1959]. Our attempts (not shown) to derive other physics-based fits to the parameters a_i led to significantly higher uncertainties than the functional forms defined by (5).

[32] Table 5 summarizes the characteristic dimensions of the model bow shocks for selected values of M_A in the same format as Table 3 to facilitate comparison between model and best fitting bow shock surfaces. Table 5 clearly shows that, in agreement with our expectations, the bow shock surface expands (y_{dusk}, y_{dawn}, and z_{north} increase) and becomes blunter with decreasing upstream Alfvénic Mach number M_A. However, the bow shock stand off distance does not change substantially. The x_{nose} distance, normalized to the average ram pressure, decreases (increases) with decreasing M_A for the GPE (GIPM) data set but the change

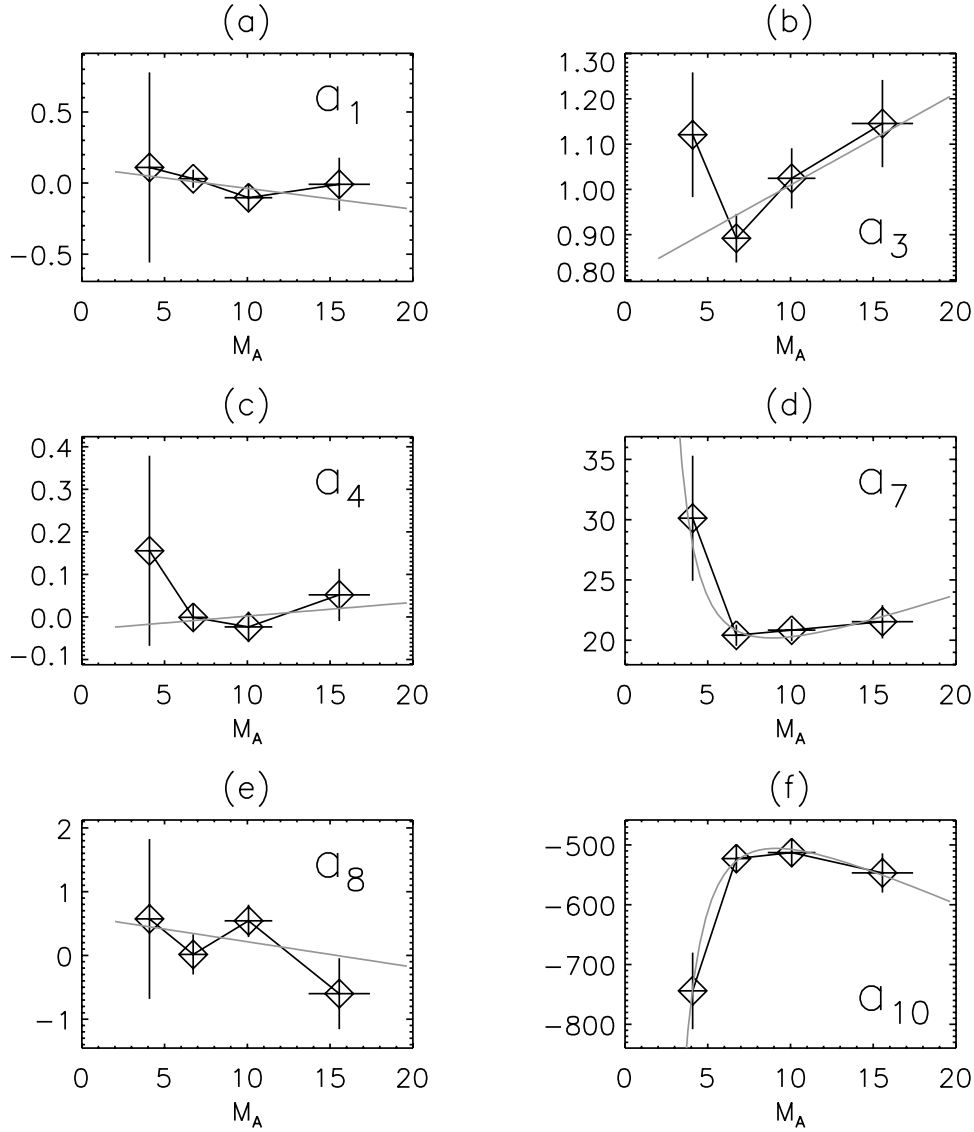

Figure 8. Same as Figure 7, but in GIPM coordinates.

is statistically insignificant because it remains within one standard deviation. Note that the uncertainties quickly increase when M_A approaches the value of 2. This is not surprising because the a_i parameters of the best fitting bow shock surface for the M_A = 2–5 subset also bear greater uncertainties than the other subsets (see Tables 2 and 3). Furthermore, additional errors have been introduced when deriving the best fits to the dependence of a_i on M_A.

[33] After a thorough analysis of the estimated errors, we come to the conclusion that in order to decrease them, a more comprehensive data set should be employed which would allow to perform finer binning, especially for Mach numbers below 5. Availability of more data points in each bin would reduce uncertainties and the finer binning would provide better guidance on what kind of functional forms to use, possibly basing the function on shock physics, contributing to a lowering of the errors. Furthermore, a larger data set will allow to account for more parameters than one (M_A) after the pressure normalization and rotation into the coordinate system of choice. For example, *Merka and Szabo* [2004] demonstrated that the shock's location is influenced by the orientation of the Earth's magnetic dipole and by the IMF orientation expressed with the θ_{Bv} angle, and that the magnitude of those effects are comparable to M_A-induced changes in bow shock position for medium and

Table 4. Coefficients b_{ij} Describing Variation in the Bow Shock Surface Parameters a_i (i = 1, 3, 4, 7, 8, 10) With M_A

i	$b_{i,1}$	$b_{i,2}$	$b_{i,3}$
		GPE Coordinates	
1	0.0063 ± 0.1649	−0.0098 ± 0.0196	
3	0.8351 ± 0.0973	0.0102 ± 0.0100	
4	−0.0298 ± 0.0627	0.0040 ± 0.0072	
7	16.39 ± 2.94	0.2087 ± 0.2280	108.3 ± 43.1
8	−0.9241 ± 0.5913	0.0721 ± 0.0591	
10	−444.0 ± 59.2	−2.935 ± 4.834	−1930 ± 618
		GIPM Coordinates	
1	0.1089 ± 0.1727	−0.0146 ± 0.0197	
3	0.8063 ± 0.1062	0.0203 ± 0.0112	
4	−0.0302 ± 0.0715	0.0032 ± 0.0075	
7	14.35 ± 4.03	0.4555 ± 0.2990	111.2 ± 67.3
8	0.6111 ± 0.6607	−0.0397 ± 0.0675	
10	−343.6 ± 75.7	−12.306 ± 6.058	−3290 ± 968

Table 5. Characteristic Dimensions of the Model Bow Shock for Various M_A Conditions

M_A	x_{nose} [R_E]	y_{dusk} [R_E]	y_{dawn} [R_E]	z_{north} [R_E]	$y_{dusk}/\lvert y_{dawn}\rvert$	y_{dusk}/z_{north}	$\lvert y_{dawn}\rvert/z_{north}$
				GPE Coordinates			
2	9.5 ± 4.1	49.6 ± 6.4	−48.0 ± 6.4	52.8 ± 7.5	1.032 ± 0.037	0.940 ± 0.033	0.910 ± 0.032
3	10.6 ± 3.3	31.3 ± 2.8	−29.9 ± 2.8	32.9 ± 3.5	1.047 ± 0.018	0.952 ± 0.017	0.909 ± 0.017
4	11.5 ± 2.8	26.5 ± 1.9	−25.3 ± 1.9	27.7 ± 2.5	1.050 ± 0.012	0.959 ± 0.012	0.913 ± 0.012
5	12.1 ± 2.7	24.6 ± 1.7	−23.5 ± 1.7	25.6 ± 2.3	1.048 ± 0.011	0.964 ± 0.012	0.920 ± 0.011
8	12.8 ± 3.2	22.9 ± 1.8	−22.2 ± 1.8	23.5 ± 2.3	1.031 ± 0.013	0.972 ± 0.015	0.943 ± 0.014
10	12.9 ± 3.5	22.5 ± 1.9	−22.1 ± 1.9	23.0 ± 2.5	1.018 ± 0.015	0.977 ± 0.018	0.959 ± 0.017
15	13.0 ± 4.4	22.2 ± 2.4	−22.5 ± 2.4	22.4 ± 2.9	0.986 ± 0.022	0.987 ± 0.028	1.001 ± 0.028
20	12.9 ± 5.3	22.0 ± 2.8	−23.1 ± 2.9	22.1 ± 3.4	0.955 ± 0.029	0.996 ± 0.040	1.043 ± 0.043
				GIPM Coordinates			
2	14.4 ± 8.5	60.0 ± 8.1	−61.0 ± 8.1	65.7 ± 9.7	0.983 ± 0.034	0.912 ± 0.033	0.928 ± 0.034
3	13.7 ± 6.1	34.2 ± 3.7	−35.2 ± 3.7	37.2 ± 4.6	0.972 ± 0.022	0.918 ± 0.023	0.945 ± 0.024
4	13.1 ± 4.5	27.1 ± 2.5	−28.0 ± 2.5	29.2 ± 3.2	0.968 ± 0.016	0.927 ± 0.018	0.958 ± 0.019
5	12.8 ± 3.9	24.3 ± 2.2	−25.1 ± 2.2	25.9 ± 2.8	0.967 ± 0.015	0.937 ± 0.017	0.969 ± 0.018
8	12.6 ± 3.9	22.3 ± 2.2	−22.9 ± 2.2	22.9 ± 2.6	0.974 ± 0.018	0.972 ± 0.022	0.997 ± 0.023
10	12.7 ± 4.2	22.3 ± 2.4	−22.7 ± 2.4	22.4 ± 2.8	0.981 ± 0.021	0.995 ± 0.026	1.014 ± 0.027
15	13.0 ± 5.0	23.3 ± 2.8	−23.4 ± 2.8	22.2 ± 3.1	0.999 ± 0.029	1.053 ± 0.038	1.055 ± 0.038
20	13.3 ± 5.9	24.7 ± 3.3	−24.3 ± 3.3	22.2 ± 3.5	1.015 ± 0.037	1.109 ± 0.052	1.093 ± 0.051

large values of M_A. Provided that a large data set were available, we could separate the dipole tilt, θ_{Bv} and M_A effects from each other, parameterize their influences properly, and then study lower order effects such as, for example, the Mach cone asymmetries at the terminator.

[34] In summary, the new models describe the bow shock surface by equation (2), where $\vec{r} = (x, y, z)$ represents the positional vector of a surface point in the GPE or GIPM coordinate system, rescaled to the average solar wind dynamic pressure according to equation (1). Although the resulting models provide a description of the bow shock shape and location for arbitrary values of P_{SW}, IMF and M_A, we recommend to use the models only for M_A values of 3–20 and at $X > -20\ R_E$ (rescaled to the average pressure). Furthermore, the models tend to underestimate bow shock nose positions for M_A values of less than 5.

4.3. Dependence on Upstream Parameters and Comparison With Other Bow Shock Models

[35] In order to estimate the performance of the newly derived bow shock models, we employed 5870 IMP 8 bow shock crossings and compared them to the models' predictions using the methodology described by *Merka et al.* [2003a] and *Merka et al.* [2005]. Note that these bow shock crossings are not averaged as in the set used in the previous sections of this study. For each observed bow shock crossing, we have calculated the bow shock position predicted by each model, R_M. The ratio of the predicted to observed bow shock positions R_M/R_O serves as a measure of the prediction accuracy. A Gaussian fit to the probability distributions of R_M/R_O was used to judge the model validity.

[36] Figures 9, 10, 11, and 12 depict variations in the models' predictions as a function of IMF and solar wind parameters. The squares in Figures 9–12 denote the center positions of the R_M/R_O distribution fits, and the vertical error bars show the half-widths. The probable errors of the fits are shown as circles with the relevant scale on the right side of the particular panel. The first fit in each panel presents predictions for all data points while the others correspond to specific upstream conditions as described by the labels. In order to facilitate comparison, gray lines are drawn through the values corresponding to the entire data set. Note that a perfect agreement of the predictions with observations would be $R_M/R_O = 1$; in order to aid the eye, dashed lines delimit the interval within ±5% from perfect agreement.

[37] Before discussing the performance of the new bow shock models, we need to establish the scope of terms average and unusual/extreme IMF/solar wind conditions within the present paper as introduced by *Merka et al.* [2003a, 2005]. The average conditions are the prevailing, or the most frequently observed, IMF/solar wind properties in the IMP 8 data set ($B < 10$ nT, $|B_X| < 5$ nT, $|B_Y| < 5$ nT, $|B_Z| < 5$ nT, $M_A > 4.5$, $M_S > 5.5$, $M_{MS} > 4$, 3 cm^{-3} $< n <$ 15 cm^{-3}, and 1.5 nPa $< P_{ram} <$ 6 nPa) while the unusual/extreme conditions denote plasma and IMF properties outside of the ranges for these average conditions.

[38] We judge the model's performance from two angles: (1) Prediction accuracy, where the perfect agreement of the predictions with observations would be $R_M/R_O = 1$; and (2) the

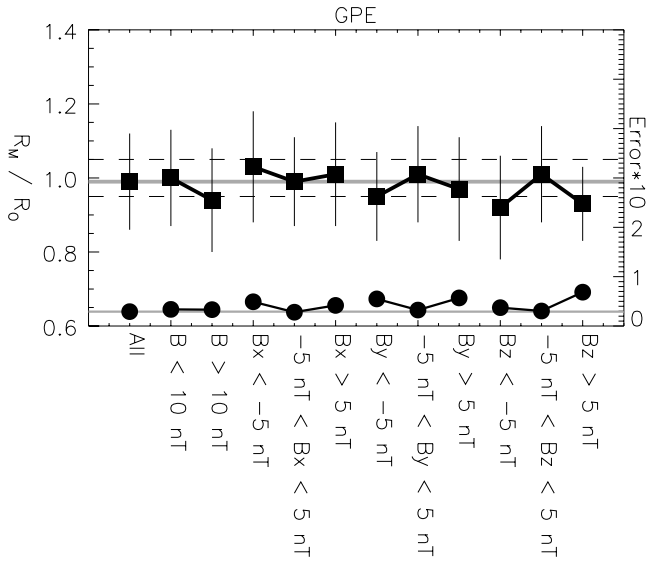

Figure 9. The ratios of predicted and observed bow shock radial distances with respect to the IMF changes for the new GPE-based bow shock model. For a description see section 4.3.

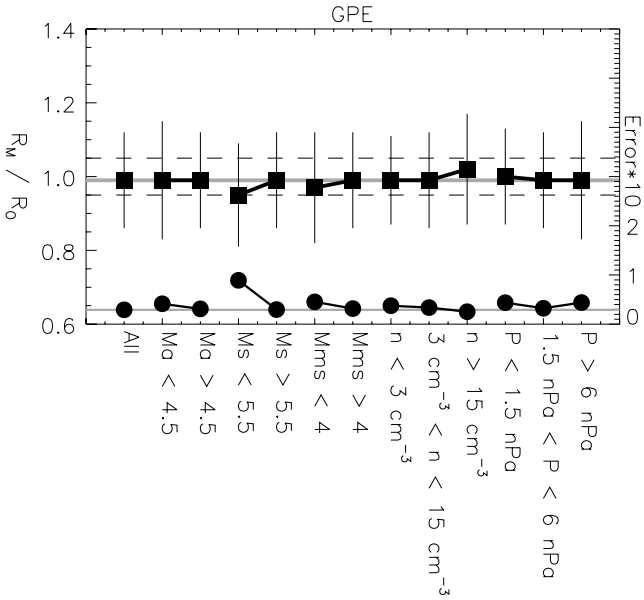

Figure 10. The ratios of predicted and observed bow shock radial distances with respect to the changes in selected plasma parameters for the new GPE-based bow shock model. For a description see section 4.3.

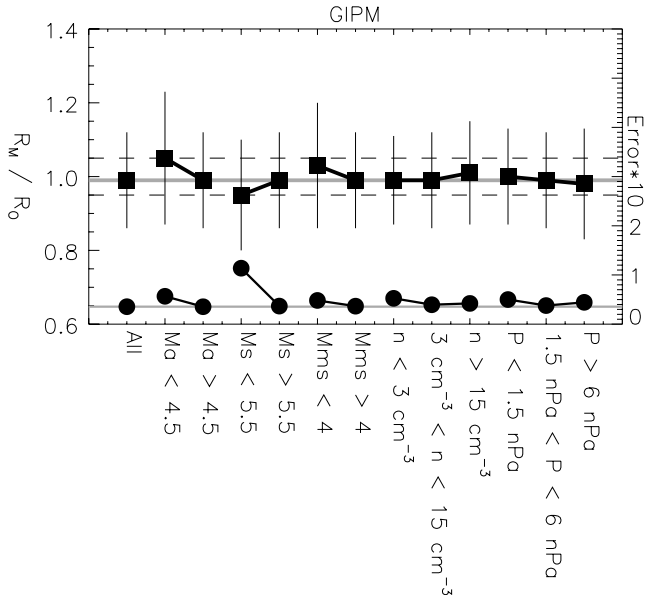

Figure 12. Same as Figure 10, but for the new GIPM-based bow shock model.

stability of the predictive capabilities for various IMF/solar wind parameter ranges. Ideally, the model would be deemed stable, or rather its predictive capabilities, if the prediction accuracy was the same for all ranges of a particular IMF/solar wind parameter.

[39] In Figures 9–12, it is readily apparent that the accuracy of the models is outstanding for the average conditions. Indeed, the predictions agree with the observations within 1% for the entire data set. On the other hand, we find larger changes in prediction accuracy (up to 8%) between the average and unusual IMF subsets (Figures 9 and 11). The model performance is remarkably good and stable for the plasma parameters (Mach numbers, plasma density, and solar wind dynamic pressure) as presented in Figures 10 and 12. The performance of the GIPM model is marginally better (by 1–2%) than of the GPE model when testing for IMF parameters but is significantly worse (by 3–5% and with larger error bars) when testing for the Mach numbers. In the light of the facts that the GIPM model compares worse with the IMP 8 bow shock crossings and that its predicted bow shock position is fraught with higher uncertainty then predictions by the GPE model, we consider the GPE model capable of providing marginally more accurate predictions of bow shock position.

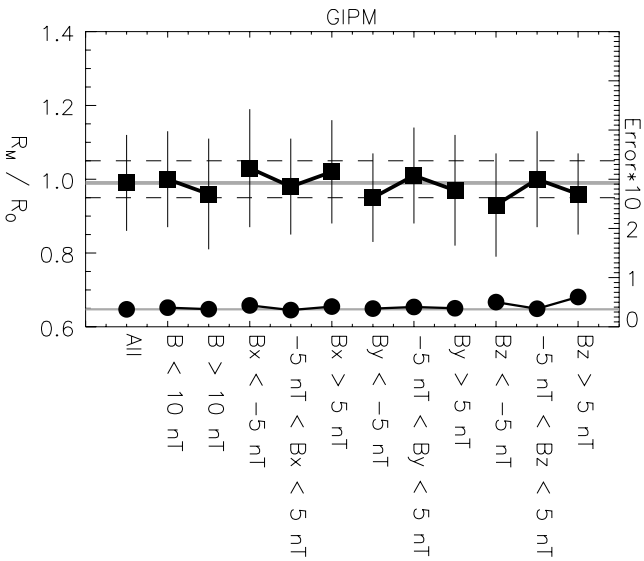

Figure 11. Same as Figure 9, but for the new GIPM-based bow shock model.

[40] The method employed to test the models and the format used in Figures 9–12 allow us to compare directly the performance of the two new models with bow shock models examined by *Merka et al.* [2005] because the method, figure format and data sets are the same. *Merka et al.* [2005] examined six bow shock models: *Formisano* [1979]; *Němeček and Šafránková* [1991]; *Farris and Russell* [1994]; *Cairns and Lyon* [1995]; *Peredo et al.* [1995]; *Verigin et al.* [2001] referred as F79, NS91, FR94, CL95, P95, and V01, respectively. Comparison of Figures 9–12 with Figures 3 and 4 of *Merka et al.* [2005] immediately reveals that the new models are more accurate although the GIPM model may be less reliable due to substantial spread of the predictions, and that their response to extreme upstream conditions is equal or better than either of the six previous bow shock models. We conclude that the best agreement between bow shock model predictions and IMP 8 observations is obtained for a wide range of upstream conditions if we use the new GPE bow shock model (out of the F79, NS91, FR94, CL95, P95, V01, and the two newly derived models).

[41] An important enhancement in the new bow shock models is the estimation of errors that provides more insight as to where to expect the bow shock. Normally, bow shock models do not provide any information about the associated uncertainties [e.g., the models examined by

Merka et al. [2005]). Without a proper error analysis, statistically insignificant features may be incorrectly interpreted and attributed to real structures and/or processes. For example, without the error analysis, one could argue that the bow shock stand off distance decreases when M_A decreases (see Figures 3 and 4). On the other hand, our error analysis shows that the observed decrease is statistically insignificant.

[42] The calculated model errors in Table 5 reflect the uncertainties embedded in the model(s) due to several contributing factors. First, the observed bow shock crossings are spread around the best fit model surface because the shock is practically never in an equilibrium position, groups of bow shock crossings were averaged when preparing the data set, and the best fit surface is only an approximation of the real unknown bow shock surface. Furthermore, the fitting procedure was performed for subsets of bow shock crossing observed under similar but not exactly the same upstream conditions, which contributes to the spread of data points around the best fit surface. Next, the uncertainties increased when we modeled the surface parameters a_i with the functional forms (5). More accurate and physics-based functional forms could be introduced if the number of observed bow shock crossings increased significantly. Table 5 shows that the model errors are significantly larger when $M_A < 3$ in comparison to $M_A > 3$ and that the predicted bow shock nose position is statistically significantly less accurate then predicted shock locations farther downstream.

[43] In spite of all the efforts, the calculated errors alone cannot account for all uncertainty sources. Probably the most important source of uncertainty unaccounted for in the error calculations is the lack of representativeness in the $M_A = 2-5$ subset of bow shock crossings where the available data only loosely constrain the best fit surface (see Figures 3 and 4). Furthermore based on theoretical considerations [*Landau and Lifshitz*, 1959] and spacecraft observations [*Russell and Zhang*, 1992; *Cairns et al.*, 1995; *Fairfield et al.*, 2001], we argue that the near-Earth orbital trajectories of the spacecraft providing the bow shock observations did not allow to observe sufficient number of data points at the shock nose for low Mach numbers (below 5) and, therefore, diminishing the models' accuracy in this region.

5. Summary and Conclusions

[44] *Peredo et al.* [1995] derived a frequently used three-dimensional bow shock model parameterized by the upstream Alfvénic Mach number from the set of approximately 550 bow shock crossings provided by 17 distinct spacecraft over the period of 1963–1980. However, several studies [e.g., *Šafránková et al.*, 1999; *Merka et al.*, 2003a, 2005] reported systematic biases in the *Peredo et al.* [1995] bow shock model predictions. Therefore we have improved upon the bow shock model of *Peredo et al.* [1995] while using their original data set and methodology and applying the bootstrap error analysis to the fitting method [e.g., *Kawano and Higuchi*, 1995; *Merka and Szabo*, 2004].

[45] We have performed three-dimensional best fits to the bow shock crossings binned by the upstream Mach numbers M_A, M_S, and M_{MS}, and found that the best fitting surfaces were best ordered with the M_A because of the greater dynamic range in M_A. In agreement with predictions from the magnetohydrodynamic theory, the bow shock surface expands when M_A decreases. The dawn-dusk asymmetry found in the bow wave is consistent with previous studies in GPE coordinates but not in GIPM coordinates, suggesting that the employed data set is not comprehensive enough to resolve this asymmetry. Nor is the Mach cone asymmetry resolved in our data set (not even in the GIPM frame).

[46] We have derived two models predicting the statistical position and shape of the bow shock in GPE or GIPM coordinates. Error analysis shows that the GPE-based model is more accurate and applicable for $M_A = 3-20$ except the nose region where the model underestimates the bow shock position for $M_A < 5$.

[47] A direct comparison of the model predictions with 5870 IMP 8 bow shock crossings demonstrated high accuracy of the predictions and, for the GPE-based model, an exceptional stability of the predictions even under extreme upstream conditions. Indeed, the new GPE-based bow shock model is more accurate and equally or more stable than the *Formisano* [1979], *Němeček and Šafránková* [1991], *Farris and Russell* [1994], *Cairns and Lyon* [1995], *Peredo et al.* [1995], or *Verigin et al.* [2001] models.

[48] The accuracy of the bow shock models could be greatly improved if the method were applied to a significantly larger data set. This would reduce the current orbital bias at the bow shock nose and would allow for multivariate parameterization of the shock surface as opposed to M_A-only parameterization. Furthermore, a larger number of bow shock crossings would likely reduce the fitting errors. Bow shock crossings observed by IMP 8, WIND, Cluster, Interball-Tail, and Geotail spacecraft could form the core of such a data set.

[49] **Acknowledgments.** The OMNI2 solar wind and IMF data were provided by the National Space Science Data Center in Greenbelt, Maryland.

[50] Shadia Rifai Habbal thanks Jacqueline Chapman and Zdenek Nemecek for their assistance in evaluating this paper.

References

Bennett, L., M. G. Kivelson, K. K. Khurana, L. A. Frank, and W. R. Paterson (1997), A model of the Earth's distant bow shock, *J. Geophys. Res.*, *102*(A12), 26,927–26,941.

Bieber, J. W., and E. C. Stone (1979), Energetic electron bursts in the magnetopause electron layer and in interplanetary space, in *Magnetospheric Boundary Layers: Proceedings of an International Conference Held in Alpbach, Austria, 11–15 June 1979*, *ESA Spec. Publ. 148*, pp. 131–135, Eur. Space Agency, Paris.

Binsack, J. H., and V. M. Vasyliunas (1968), Simultaneous IMP 2 and OGO I observations of bow shock compression, *J. Geophys. Res.*, *73*(1), 429.

Cairns, I. H., and C. L. Grabbe (1994), Towards an MHD theory for the standoff distance of Earth's bow shock, *Geophys. Res. Lett.*, *21*(25), 2781–2784.

Cairns, I. H., and J. G. Lyon (1995), MHD simulations of Earth's bow shock at low Mach numbers: Standoff distances, *J. Geophys. Res.*, *100*(A9), 17,173–17,180.

Cairns, I. H., and J. G. Lyon (1996), Magnetic field orientation effects on the standoff distance of Earth's bow shock, *Geophys. Res. Lett.*, *23*(21), 2883–2886.

Cairns, I. H., D. H. Fairfield, R. R. Anderson, V. E. H. Carlton, K. I. Paularena, and A. J. Lazarus (1995), Unusual locations of Earth's bow shock on September 24–25, 1987: Mach number effects, *J. Geophys. Res.*, *100*(A1), 47–62.

Chao, J. K., D. J. Wu, C.-H. Lin, Y. H. Yang, X. Y. Wang, M. Kessel, S. H. Chen, and R. P. Lepping (2002), Models for the size and shape of the Earth's magnetopause and bow shock, in *Space Weather Study Using Multipoint Techniques, Proceedings of the COSPAR Colloquium held in Pacific Green Bay, Wanli, Taipei, Taiwan, 27–29 September, 2000*, edited by L.-H. Lyu, p. 127, Elsevier, New York.

Chapman, J. F., and I. H. Cairns (2003), Three-dimensional modeling of Earth's bow shock: Shock shape as a function of Alfvén Mach number, *J. Geophys. Res.*, *108*(A5), 1179, doi:10.1029/2001JA000219.

Chapman, J. F., I. H. Cairns, J. G. Lyon, and C. R. Boshuizen (2004), MHD simulations of Earth's bow shock: Interplanetary magnetic field orientation effects on shape and position, *J. Geophys. Res.*, *109*, A04215, doi:10.1029/2003JA010235.

De Sterck, H., B. C. Low, and S. Poedts (1998), Complex magnetohydrodynamic bow shock topology in field-aligned low-β flow around a perfectly conducting cylinder, *Phys. Plasmas*, *5*(11), 4015–4027.

Dmitriev, A. V., J. K. Chao, and D.-J. Wu (2003), Comparative study of bow shock models using Wind and Geotail observations, *J. Geophys. Res.*, *108*(A12), 1464, doi:10.1029/2003JA010027.

Efron, B. (1979), Bootstrap methods: Another look at the jackknife, *Ann. Stat.*, *7*, 1–26.

Fairfield, D. H. (1971), Average and unusual locations of the Earth's magnetopause and bow shock, *J. Geophys. Res.*, *76*(28), 6700–6715.

Fairfield, D. H., I. H. Cairns, M. D. Desch, A. Szabo, A. J. Lazarus, and M. R. Aellig (2001), The location of low Mach number bow shock at Earth, *J. Geophys. Res.*, *106*(A11), 25,361–25,376.

Farris, M. H., and C. T. Russell (1994), Determining the standoff distance of the bow shock: Mach number dependence and use of models, *J. Geophys. Res.*, *99*(A9), 17,681–17,689.

Farris, M. H., S. M. Petrinec, and C. T. Russell (1991), The thickness of the magnetosheath: Constraints on the polytropic index, *Geophys. Res. Lett.*, *18*(10), 1821–1824.

Formisano, V. (1979), Orientation and shape of the Earth's bow shock in three dimensions, *Planet. Space Sci.*, *27*(9), 1151–1161.

Holzer, R. E., and J. A. Slavin (1978), Magnetic flux transfer associated with expansions and contractions of the dayside magnetosphere, *J. Geophys. Res.*, *83*, 3831.

Kabin, K. (2001), A note on the compression ratio in MHD shocks, *J. Plasma Phys.*, *66*(4), 259–274.

Kawano, H., and T. Higuchi (1995), The bootstrap method in space physics: Error estimation for the minimum variance analysis, *Geophys. Res. Lett.*, *22*(3), 307–310.

Ku, H. (1966), Notes on the use of propagation of error formulas, *J. Res. Natl. Bur. Stand. U.S., Sect. C*, *70*(4), 263–273.

Landau, L. D., and E. M. Lifshitz (1959), *Fluid Mechanics*, pp. 310–313, Elsevier, New York.

Marquardt, D. W. (1963), An algorithm for least-squares estimation of nonlinear parameters, *J. Soc. Indust. Appl. Math.*, *11*, 431–441.

Merka, J., and A. Szabo (2004), Bow shock's geometry at the magnetospheric flanks, *J. Geophys. Res.*, *109*, A12224, doi:10.1029/2004JA010567.

Merka, J., A. Szabo, T. W. Narock, J. H. King, K. I. Paularena, and J. D. Richardson (2003a), A comparison of IMP 8 observed bow shock positions with model predictions, *J. Geophys. Res.*, *108*(A2), 1077, doi:10.1029/2002JA009384.

Merka, J., A. Szabo, J. Šafránková, and Z. Němeček (2003b), Earth's bow shock and magnetopause in the case of a field-aligned upstream flow: Observation and model comparison, *J. Geophys. Res.*, *108*(A7), 1269, doi:10.1029/2002JA009697.

Merka, J., A. Szabo, T. W. Narock, J. D. Richardson, and J. H. King (2005), Three decades of bow shock observations by IMP 8 and model predictions, *Planet. Space Sci.*, *53*(1–3), 79–84, doi:10.1016/j.pss.2004.09.031.

Němeček, Z., and J. Šafránková (1991), The Earth's bow shock and magnetopause position as a result of the solar wind-magnetosphere interaction, *J. Atmos. Terr. Phys.*, *53*, 1049–1054.

Němeček, Z., M. Hayosh, J. Šafránková, G. N. Zastenker, and J. D. Richardson (2003), The dawn-dusk asymmetry of the magnetosheath: Interball-1 observations, *Adv. Space Res.*, *31*(5), 1333–1340, doi:10.1016/S0273-1177(03)00007-3.

Paularena, K. I., J. D. Richardson, M. A. Kolpak, C. R. Jackson, and G. L. Siscoe (2001), A dawn-dusk density asymmetry in Earth's magnetosheath, *J. Geophys. Res.*, *106*(A11), 25,377–25,394.

Peredo, M., D. P. Stern, and N. A. Tsyganenko (1993), Are existing magnetospheric models excessively stretched?, *J. Geophys. Res.*, *98*(A9), 15,343–15,354.

Peredo, M., J. A. Slavin, E. Mazur, and S. A. Curtis (1995), Three-dimensional position and shape of the bow shock and their variation with Alfvénic, sonic and magnetosonic Mach numbers and interplanetary magnetic field orientation, *J. Geophys. Res.*, *100*(A5), 7907–7916.

Petrinec, S. M., and C. T. Russell (1997), Hydrodynamic and MHD equations across the bow shock and along the surfaces of planetary obstacles, *Space Sci. Rev.*, *79*(3–4), 757–791.

Romanov, S. A., V. N. Smirnov, and O. L. Vaisberg (1978), Interaction of the solar wind with Venus, *Cosmic Res., Engl. Trans.*, *16*, 603.

Russell, C. T., and T. L. Zhang (1992), Unusually distant bow shock encounters at Venus, *Geophys. Res. Lett.*, *19*, 833–836.

Šafránková, J., Z. Němeček, and M. Borák (1999), Bow shock position: Observations and models, in *Interball in the ISTP Program, Studies of the Solar Wind-Magnetopause-Ionosphere Interaction*, *NATO Sci. Ser.*, *537*, edited by D. G. Sibeck and K. Kudela, pp. 187–201, Springer, New York.

Slavin, J. A., and R. E. Holzer (1981), Solar wind flow about the terrestrial planets:1. Modeling bow shock position and shape, *J. Geophys. Res.*, *86*, 11,401–11,418.

Slavin, J. A., R. E. Holzer, J. R. Spreiter, S. S. Stahara, and D. S. Chaussee (1983), Solar wind flow about the terrestrial planets: 2. Comparison with gas dynamic theory and implications for solar-planetary interactions, *J. Geophys. Res.*, *88*(A1), 19–35.

Slavin, J. A., R. E. Holzer, J. R. Spreiter, and S. S. Stahara (1984), Planetary Mach cones: Theory and observation, *J. Geophys. Res.*, *89*(A5), 2708–2714.

Slavin, J. A., A. Szabo, M. Peredo, C. J. Owen, R. P. Lepping, R. Fitzenreiter, R. W. Ogilvie, J. L. Stremberg, and A. J. Lazarus (1996), Near-simultaneous bow shock crossings by Wind and IMP 8 on December 1, 1994, *Geophys. Res. Lett.*, *23*(10), 1207–1210.

Spreiter, J. R., and A. W. Rizzi (1974), Aligned MHD solution for solar wind flow past the Earth's magnetosphere, *Acta Astronaut.*, *1*(1–2), 15–35.

Spreiter, J. R., and S. S. Stahara (1985), Magnetohydrodynamic and gas-dynamic theories for planetary bow waves, in *Collisionless Shocks in the Heliosphere: Reviews of Current Research*, *Geophys. Monogr. Ser.*, vol. 35, edited by B. T. Tsurutani and R. G. Stone, pp. 85–107, AGU, Washington, D. C.

Spreiter, J. R., A. L. Summers, and A. Y. Alksne (1966), Hydromagnetic flow around the magnetosphere, *Planet. Space Sci.*, *14*, 223–253.

Verigin, M., G. Kotova, A. Szabo, J. Slavin, T. Gombosi, K. Kabin, F. Shugaev, and A. Kalinchenko (2001), WIND observations of the terrestrial bow shock: 3-D shape and motion, *Earth Planets Space*, *53*(10), 1001–1009.

Verigin, M., J. A. Slavin, A. Szabo, G. Kotova, and T. Gombosi (2003), Planetary bow shocks: Asymptotic MHD Mach cones, *Earth Planets Space*, *55*, 33–38.

Walters, G. K. (1964), Effect of oblique interplanetary magnetic field on shape and behaviour of the magnetosphere, *J. Geophys. Res.*, *69*(9), 1769–1783.

J. Merka, J. A. Slavin, and A. Szabo, NASA Goddard Space Flight Center, Laboratory for Solar and Space Physics, Code 612.3, Greenbelt, MD 20771, USA. (jan.merka@gsfc.nasa.gov; james.a.slavin@nasa.gov; adam.szabo@gsfc.nasa.gov)

M. Peredo, SSAI, 10210 Greenbelt Road, Suite 500, Lanham, MD 20706, USA. (mauricio_peredo@ssaihq.com)